

Rotation invariant point cloud analysis: Where local geometry meets global topology

Chen Zhao^a, Jiaqi Yang^b, Xin Xiong^a, Angfan Zhu^a, Zhiguo Cao^{a,*}, Xin Li^c

^aNational Key Laboratory of Science and Technology on Multi-spectral Information Processing, School of Artificial Intelligence and Automation, Huazhong University of Science and Technology, Wuhan, 430074, China

^bSchool of Computer Science, Northwestern Polytechnical University, Xi'an, 710072, China

^cLane Department of Computer Science and Electrical Engineering, West Virginia University, Morgantown, 26506, USA

Abstract

Point cloud analysis is a fundamental task in 3D computer vision. Most previous works have conducted experiments on synthetic datasets with well-aligned data; while real-world point clouds are often not pre-aligned. How to achieve rotation invariance remains an open problem in point cloud analysis. To meet this challenge, we propose an approach toward achieving rotation-invariant (RI) representations by combining local geometry with global topology. In our local-global-representation (LGR)-Net, we have designed a two-branch network where one stream encodes local geometric RI features and the other encodes global topology-preserving RI features. Motivated by the observation that local geometry and global topology have different yet complementary RI responses in varying regions, two-branch RI features are fused by an innovative multi-layer perceptron (MLP) based attention module. To the best of our knowledge, this work is the first principled approach toward adaptively combining global and local information under the context of RI point cloud analysis. Extensive experiments have demonstrated that our LGR-Net achieves the state-of-the-art performance on various rotation-augmented versions of ModelNet40, ShapeNet, ScanObjectNN, and S3DIS.

Keywords: Point cloud analysis, rotation invariance, deep learning, classification, segmentation

1. Introduction

3D computer vision has been playing a pivotal role in many real-world applications -e.g., autonomous driving [20, 27, 46, 6], augmented reality [1, 23], and robotics [10, 4]. As a basic type of 3D data representation, point cloud analysis has received increasingly more attention in 3D vision. One of the pioneering works of deep learning based point cloud analysis, PointNet [29], employs multi-layer perceptron (MLP) to extract salient features from raw 3D coordinates. Unfortunately, most previous works are evaluated on synthetic datasets such as ModelNet40 [44] and ShapeNet [47], where point cloud models are assumed to be pre-aligned. Nonetheless, it is seldom the case to access well-aligned point clouds in real world applications, where geometric transformations are inevitable. In fact, the pose of point cloud models is often arbitrary in practice - it might include simple translation or complex 3D rotations or both. The performance of PointNet and its modified versions [31, 45, 42] degrades rapidly due to the change of coordinates (caused by unknown geometric transformations). As shown in Fig. 1(a), the accuracy of PointNet on both classification and segmentation significantly deteriorates in the presence of small rotations.

Note that translation invariance can be easily achieved by recentering point clouds. By contrast, rotation invariance is

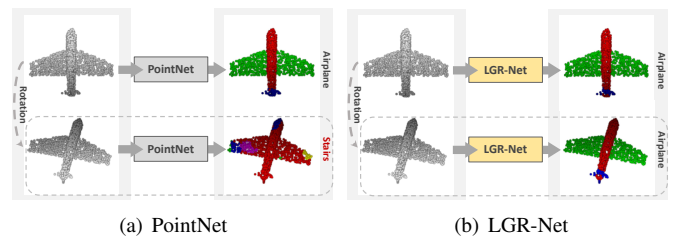


Figure 1: The proposed LGR-Net is rotation-invariant as compared to PointNet. The segmentation and classification results generated by PointNet (a) are considerably affected by the rotation; while the results of our LGR-Net (b) are invariant.

more challenging and has attracted increasingly more attention in recent years [48, 5]. An intuitive solution to address the issue of rotation-invariant (RI) analysis is to augment the training data by considering all possible rotations. However, such ad-hoc strategy is practically infeasible because the space of all 3D rotations is too large to sample. Another sensible approach is to use Spherical Fourier Transform (SFT) [41] on spheres to achieve rotation equivariance [11, 7]. Despite its theoretical appeal, discrete implementation of SFT is nontrivial (the loss of information is inevitable during the projection) and spherical CNNs often require extra processing (e.g., max pooling) to achieve rotation invariance. Alternatively, one can consider the pursuit of RI representations for point cloud analysis. The spatial coordinates of point clouds might change with rotations; but geometric attributes such as distances and angles do not vary. Indeed, RI representations have been considered

*Corresponding author.

Email addresses: hust_zhao@hust.edu.cn (Chen Zhao), jqqyang@nwpu.edu.cn (Jiaqi Yang), xiong_xin@hust.edu.cn (Xin Xiong), zhuangfan@hust.edu.cn (Angfan Zhu), zgcao@hust.edu.cn (Zhiguo Cao), Xin.Li@mail.wvu.edu (Xin Li)

most recently [48, 5]. However, existing methods have primarily focused on utilizing geometric shape attributes in local regions only; while their distinctiveness is often questionable in the presence of symmetric structures (e.g., planes) (refer to Fig. 3). The potential of exploiting global topology-related RI representations has been largely overlooked as far as we know.

In this paper, we present a simple yet effective solution to RI point cloud analysis by combining local geometry and global topology information in a principled manner. When compared against PointNet, our method dubbed LGR-Net is fully invariant to the rotation in both classification and segmentation tasks (as shown in Fig. 1(b)). For local representations, we have extended persistent feature histograms [32] into a more distinctive feature space, where the shape attributes in a local region around the query point are determined by a Darboux frame [35]. For global representations, we generate RI spatial locations by projecting original points onto a rotation-equivariant global coordinate system established from the down-sampled skeleton-like structure [37, 16]. We both rigorously and experimentally show that our local and global representations (LGR) can achieve the desirable rotation invariance. In order to extract RI features from the LGR, we propose a two-branch network where the local and global information are separately processed and then adaptively combined by an attention-based fusion. The rationale behind the attention-based adaptive fusion can be justified by contrasting a point in a flat region with a point around a corner (refer to Fig. 3) - for the former, local information is clearly insufficient for classification or segmentation; while for the latter, local information is already amenable to describing the distinctive local structures. Extensive experimental results are reported for both synthetic datasets (ModelNet40 [44] and ShapeNet [47]) and real-world datasets (ScanObjectNN [40] and S3DIS [3]) to show that our approach has achieved remarkably superior performance on rotation-augmented benchmark datasets. In a nutshell, our major contributions are summarized as follows:

- We present LGR-Net which considers local geometric features and global topology-preserving features to achieve rotation invariance. The complementary relationship between shape descriptions and spatial attributes is cleverly exploited by our two-branch network, and their strengths are adaptively combined by an attention-based fusion module.
- Our approach¹ achieves impressive experimental results when compared with current state-of-the-art methods on both synthetic and real-world datasets undergoing random 3D rotations. The performance improvements are particularly striking in the presence of complex rotations (e.g., $S O 3$ group [2]).

¹Code is made available at <https://github.com/sailor-z/LGR-Net>.

2. Related Work

Spatial transformations. In early works, a straightforward approach is to augment the training data using transformations of arbitrary rotations [29, 31]. However, since 3D rotations include three degrees of freedom -i.e., pitch, yaw, and roll, sampling them from 0-degree to 360-degree results in astronomical number of data points. Consequently, it is often impractical to cover all possible rotations in real-world applications. An alternative yet more efficient approach employs deep learning methods to directly learn the unknown spatial transformations [29]. Specifically, T-Net has been used in PointNet to regress a 3×3 spatial transformation and a 64×64 high-dimensional transformation, targeting at transforming point clouds into a canonical coordinate system. Nevertheless, PointNet with the learned transformations is still vulnerable to the nuisance of rotations as shown in Sec. 4.

Rotation equivariance convolutions. Inspired by the popularity of convolutional neural networks in 2D computer vision, several works have been developed to leverage the success of convolutions from image data to point clouds [45, 22, 42]. However, most previous works did not take rotation invariance into account and therefore were sensitive to rotations. Some works have utilized spherical convolutions to achieve rotation equivariance [11, 7, 24]. Note that the equivariance means the output and the input vary equally, which is intrinsically different from invariance. Additional process such as max pooling becomes necessary in order to achieve rotation invariance. Moreover, the loss of information is inevitable during the generation of mesh/voxel, the transform and inverse transform, which limits the overall performance in practical implementations.

Rotation-invariant representations. The third class of approaches attempt to transform the raw point clouds into rotation-invariant representations. Among RI representations, distances and angles are the most widely used features. Specifically, a 4D point pair feature (PPF) was proposed in [8] for the task of RI descriptors, which utilized the distances and angles between the central reference point and neighbors in a local patch. For the tasks of classification and segmentation, [5] integrated distance, angle, \sin , and \cos features in local kNN-graphs into a cluster network; [48] combined distance and angle features in local graphs and those in reference points generated by down sampling. We note that all previous works concentrated on local features -i.e., relative distances and angles in local graphs. However, local information is inevitably ambiguous for the tasks of classification and segmentation. For instance, the geometric shape descriptions represented by distances and angles tend to be similar among different points in the same plane (refer to Fig. 3). Along this line of reasoning, absolute spatial attributes in a global coordinate system are critical to resolve location uncertainty.

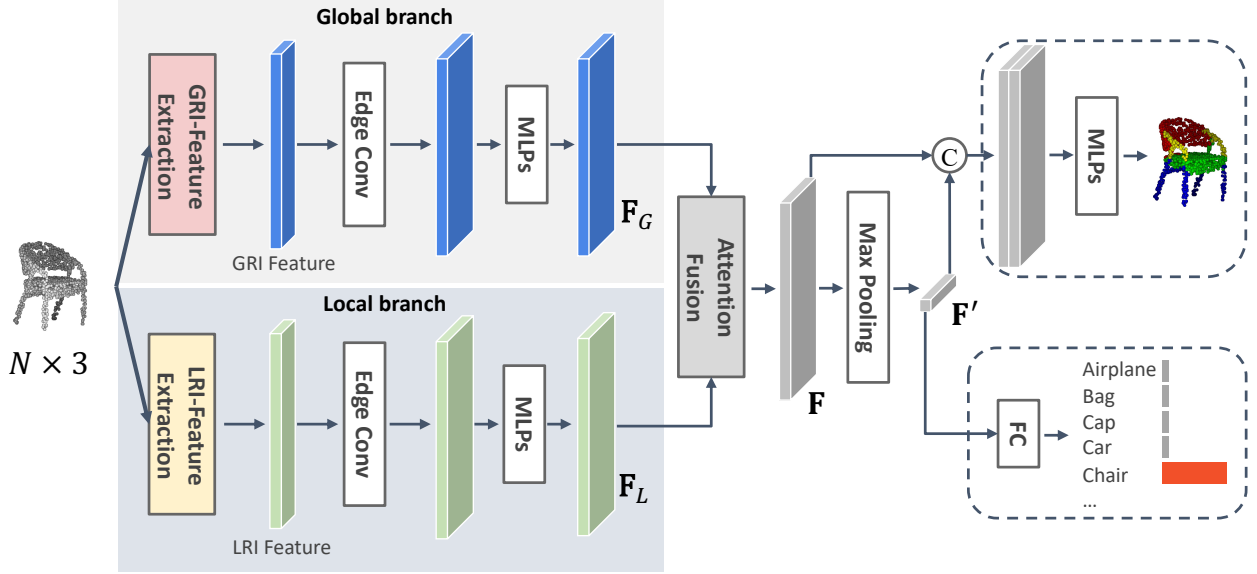


Figure 2: Network architecture. The architecture includes two branches that consume raw 3D points $\mathbf{P} \in \mathbb{R}^{N \times 3}$ to separately generate local and global representations. High-dimensional features ($\mathbf{F}_G, \mathbf{F}_L$) are extracted by MLPs and then fused into a feature embedding (\mathbf{F}) by an attention-based fusion module.

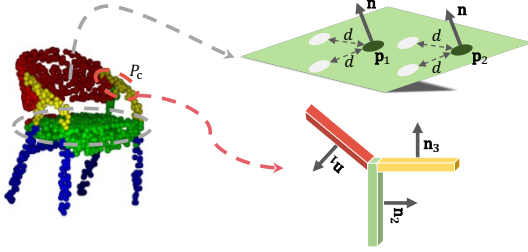


Figure 3: Effectiveness of local geometry in different regions. ($\mathbf{p}_1, \mathbf{p}_2$) are located on the same plane with the normal \mathbf{n} , while P_c is a set of corner points. d represents the Euclidean distance. The same Euclidean distances and normals lead to ambiguous local descriptions around \mathbf{p}_1 and \mathbf{p}_2 ; while the local context around P_c is distinctive.

3. Proposed Method

Fig. 2 shows the architecture of our LGR-Net. 3D points are consumed by a two-branch network to separately generate local and global RI representations. An attention-based fusion module is proposed to fuse the local and global features in an adjustable manner. The superiority of our separation-and-fusion design is introduced in Sec. 4.8.

3.1. Problem Statement

Our method directly works with raw point cloud data, which are represented as a matrix of 3D coordinates $\mathbf{P} \in \mathbb{R}^{N \times 3}$ - i.e., $\mathbf{P} = [\mathbf{p}_1; \mathbf{p}_2; \dots; \mathbf{p}_n]$ with $\mathbf{p}_i = (x_i, y_i, z_i)$. The normal of each point is denoted by $\mathbf{n}_i = (n_x^i, n_y^i, n_z^i)$. The issue of rotation invariance can be formulated by transforming \mathbf{P} through a 3×3 orthogonal matrix $\mathbf{R} \in SO(3)$ ($\det(\mathbf{R}) = 1$), which contains three degrees of freedom - i.e., $\alpha \in [0, 2\pi], \beta \in [0, \pi]$, and $\gamma \in [0, 2\pi]$. The objective of achieving rotation invariance then boils down to

$$\mathcal{F}(\mathbf{P}\mathbf{R}) = \mathcal{F}(\mathbf{P}), \quad (1)$$

where $\mathcal{F} : \mathbb{R}^{N \times 3} \rightarrow \mathbb{R}^{N \times D}$. For the classification task, the desirable output is s scores among which the maximum is expected to be the correct class label. For the segmentation task, the output is a $N \times m$ map whose entries indicate the scores of m categories. Our objective is to achieve invariance to 3D rotations in both tasks.

3.2. Local Branch

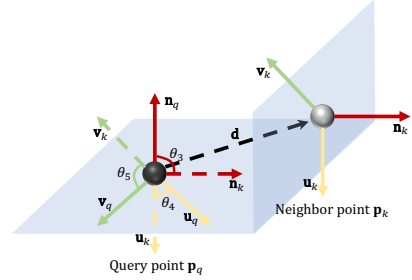


Figure 4: LRI (local-rotation-invariant)-feature extraction in the local branch. Given a query point \mathbf{p}_q and its neighbors (\mathbf{p}_k as an example), the local geometric shape is described by the relative distance $\|\mathbf{d}\|$ and high-order relationships between local coordinates $(\mathbf{n}_q, \mathbf{u}_q, \mathbf{v}_q)$ and $(\mathbf{n}_k, \mathbf{u}_k, \mathbf{v}_k)$, where $(\mathbf{n}_q, \mathbf{n}_k)$ are the normals of $(\mathbf{p}_q, \mathbf{p}_k)$, and other axes are located by cross product.

In previous works, local features have been proven critical to the tasks of point cloud classification and segmentation [45, 22, 42], because local features are capable of describing geometric shape attributes in local regions. Taking rotation invariance into account, we employ the relative distances and angles as basic local descriptors, whose RI property can be easily verified. In order to have a richer collection of local shape descriptions, we consider an extended Darboux frame [32, 35] by characterizing higher-order relationships among RI geometric attributes (distances and angles) as follows.

As shown in Fig. 4, For a query point \mathbf{p}_q , a local graph is generated by k-nearest neighbor (kNN) searching, and we assume a neighbor point \mathbf{p}_k to be one of the kNNs. The relative position between \mathbf{p}_q and \mathbf{p}_k is described as $\|\mathbf{d}\|$ ($\mathbf{d} = \mathbf{p}_k - \mathbf{p}_q$). However, the location of \mathbf{p}_k is ambiguous without taking orientation into account. Consequently, we estimate the orientation of \mathbf{p}_k by calculating the higher-order relationships between the local coordinates centered at \mathbf{p}_q and \mathbf{p}_k . Specifically, the local frame (e.g., $(\mathbf{n}_q, \mathbf{u}_q, \mathbf{v}_q)$) is generated as

$$\mathbf{u}_q = \mathbf{d} \times \mathbf{n}_q, \quad (2)$$

$$\mathbf{v}_q = \mathbf{u}_q \times \mathbf{n}_q, \quad (3)$$

where \times denotes cross product. The septuplet $[\mathbf{d}, (\mathbf{n}_q, \mathbf{u}_q, \mathbf{v}_q), (\mathbf{n}_k, \mathbf{u}_k, \mathbf{v}_k)]$ then serves as the building block for characterizing higher-order relative relationship. The orientation of \mathbf{p}_k is computed by a 7-dimensional vector $\{\theta_1, \theta_2, \theta_3, \theta_4, \theta_5, \theta_6, \theta_7\}$, in which each entry denotes the angle between a pair of feature descriptors $(\mathbf{d}, \mathbf{n}_q)$, $(\mathbf{d}, \mathbf{n}_k)$, $(\mathbf{n}_q, \mathbf{n}_k)$, $(\mathbf{u}_q, \mathbf{u}_k)$, $(\mathbf{v}_q, \mathbf{v}_k)$, $(\mathbf{u}_q, \mathbf{v}_k)$, $(\mathbf{v}_q, \mathbf{u}_k)$, respectively. Moreover, each angle descriptor is defined by the *cos* similarity between two low-order feature descriptors - taking θ_1 as an example, we have

$$\cos(\theta_1) = \frac{\mathbf{d} \cdot \mathbf{n}_q}{\|\mathbf{d}\| \|\mathbf{n}_q\|}. \quad (4)$$

Note that θ_6 and θ_7 are included to resolve the ambiguity arising from the orientation of local surfaces. Given k nearest neighbors for a query point \mathbf{p}_q , a $k \times 8$ RI representation is generated which comprehensively characterizes the local pairwise relative relationships around \mathbf{p}_q while satisfies minimum redundancy requirement.

It is worth noting that normals are employed in the local branch for local frame estimation instead of pure information enrichment. In previous works [29, 31], normals are immediately concatenated with 3D coordinates to enrich the input information, which is vulnerable against rotations (Please refer to PointNet (*xyz + normal*) in Table 1). By contrast, normals are reasonably utilized in our local branch to estimate local RI features which are not only capable of describing local geometric structures, but also invariant to rotations.

3.3. Global Branch

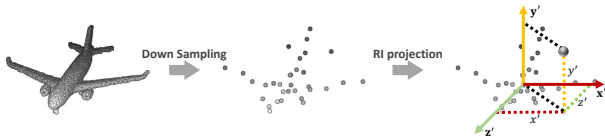


Figure 5: GRI (global-rotation-invariant)-feature extraction in the global branch. A rotation equivariance coordinate system is generated from a skeleton-like structure. Raw points are then projected onto the generated frame, which leads to rotation-invariant spatial locations.

Although geometric attributes in local regions have been studied in RI point cloud analysis, the issue of exploiting absolute spatial information has largely remained open. [48] suggests that the classification result significantly increases on

rotation-free datasets when the presented (RI) representations are replaced with raw 3D coordinates, while the method is no longer robust to rotation. As shown in Fig. 3, working with local feature descriptors alone is often insufficient due to the lack of distinctive spatial attributes such as absolute locations. Considering the points located on a plane, local geometric attributes (e.g., distances and angles) tend to be similar and cause inevitable confusion. Therefore, the rotation-invariant spatial attributes are expected to eliminate the ambiguity.

An intuitive solution to characterize spatial attributes is to work with point locations in a global coordinate system. However, the raw locations are sensitive to rotations. In order to acquire rotation-invariant spatial attributes, we employ singular value decomposition (SVD) [13] which is a promising strategy capable of seeking canonical rotation-equivariant directions. Nevertheless, as shown in [19], exploiting second-order shape information does not guarantee the optimal alignment. Moreover, it is noise-sensitive and time-consuming to directly apply SVD to the original point cloud model which may contain thousands of points. For the sake of an efficient and robust solution, we propose to down-sample the original point cloud, while preserving the global topological structure -i.e., skeleton-like structure as shown in Fig. 5. The actual down-sampling procedure is implemented by farthest point sampling [28] in our experiments. The robustness of our down-sampled SVD strategy against nuisances can be found in Table 2 and Table 6.

Then we carry out SVD on the down-sampled structure \mathbf{P}_d which is formulated as

$$\mathbf{U}\mathbf{\Sigma}\mathbf{V}^T = \mathbf{P}_d, \quad (5)$$

where \mathbf{V} contains the three orthogonal axes which are equivariant to rotations. To achieve rotation invariance, points are transformed from the original model to the newly-established global coordinate system as

$$\hat{\mathbf{P}} = \mathbf{P} \cdot \mathbf{V}, \quad (6)$$

where $\hat{\mathbf{P}}$ describes the desired spatial RI attributes. Rigorous proof about rotation invariance of SVD-based transformation can be found in Sec. 3.5. Moreover, since the raw SVD technique is vulnerable to sign flipping, we address this issue by a simple yet effective solution. Specifically, we determine the final directions of three axes by estimating the angles between each axis and a predefined anchor point (the farthest point from the centroid in our experiments). As shown in Fig. 6, the axis will be flipped if the corresponding angle is larger than 90° .

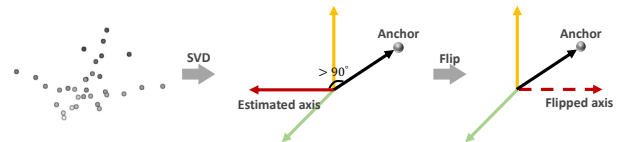


Figure 6: Illustration of determining the final directions of axes in the global branch.

3.4. Attention-based Fusion

In order to generate an overall feature embedding (\mathbf{F}) from a pair of feature maps ($\mathbf{F}_G, \mathbf{F}_L$) produced by local and global branches, we suggest combining them by attention-based fusion [15]. An intuitive approach is to pool together the information by either average or max operation which has been widely used [9, 34, 14]. However, considering the complementary nature of local and global attributes, it is more reasonable to adaptively combine the information contained in these two branches.

As illustrated in Fig. 3, for points ($\mathbf{p}_1, \mathbf{p}_2$) located on a plane, local geometric attributes are often ambiguous because of the same relative distances and normals. In this case, the spatial characteristics of ($\mathbf{p}_1, \mathbf{p}_2$) described in the global branch are preferred over the local counterpart. By contrast, for the set of points \mathbf{P}_c located around a corner, the local geometric context is distinctive enough and therefore expected to play a more significant role. Inspired by this observation, we have designed a multi-layer perception (MLP) module for attention-based fusion that adaptively integrates two-branch features as follows.

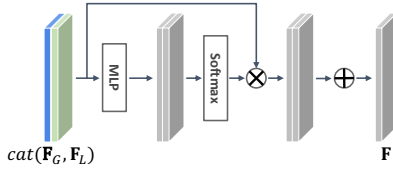


Figure 7: Architecture of the attention-based fusion module.

As shown in Fig. 7, \mathbf{F}_G and \mathbf{F}_L are first concatenated and embedded by MLP. Second, a softmax layer is used to estimate the response weights by (\mathbf{w}_G as an example)

$$\mathbf{w}_G^i = \frac{e^{\mathbf{f}_G^i}}{e^{\mathbf{f}_G^i} + e^{\mathbf{f}_L^i}}, \quad (7)$$

where \mathbf{w}_G^i is the global-branch weight of \mathbf{p}_i and ($\mathbf{f}_G^i, \mathbf{f}_L^i$) denote embedded features of \mathbf{p}_i . Third, the attention-based fusion result \mathbf{F} is generated by

$$\mathbf{F} = \mathbf{w}_G \mathbf{F}_G + \mathbf{w}_L \mathbf{F}_L. \quad (8)$$

Another plausible strategy is immediately concatenating two-branch features and fusing them by MLPs. We empirically suggest that our attention fusion is superior over such strategy as well as the pooling processing (Please refer to Table 8).

3.5. Rotation-Invariant Analysis

As demonstrated in Fig. 8, we visualize the extracted global and local representations in the 3D space using *t-SNE* [25]. It is straightforward to observe that raw point locations in Fig. 8 (a) are sensitive to orientation changes; while the projected locations of our representations in Fig. 8 (b) are immune to the challenge of rotations. A rigorous justification about the RI properties of distance, angle and SVD transformation is given below.

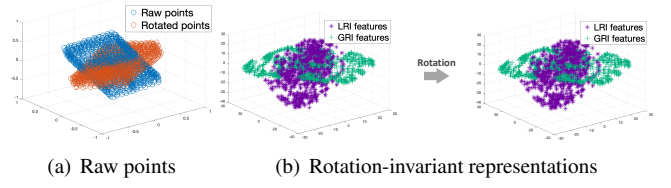


Figure 8: Comparison of the robustness against rotations between (a) raw points and (b) presented rotation-invariant representations. RI representations are visualized in 3D space by *t-sne* [25]. Under two different orientations, the raw coordinates of 3D points are significantly changed; while our global and local representations are invariant.

Distance. Assuming (d, d') is the L_2 norm of $(\mathbf{p}, \mathbf{p}')$, where $\mathbf{p}' = \mathbf{p}\mathbf{R}$ ($\mathbf{p} \in \mathbb{R}^{1 \times 3}$), the invariance against rotation is able to be proved as

$$d' = \|\mathbf{p}\mathbf{R}\| = \mathbf{p}\mathbf{R}\mathbf{R}^T\mathbf{p}^T = d. \quad (9)$$

Angle. Supposing $(\theta_{ij}, \theta'_{ij})$ are the angles between $(\mathbf{p}_i, \mathbf{p}_j)$ and $(\mathbf{p}'_i, \mathbf{p}'_j)$, the equivalence is formulated as

$$\cos(\theta'_{ij}) = \frac{\mathbf{p}'_i \mathbf{p}'_j{}^T}{\|\mathbf{p}'_i\| \|\mathbf{p}'_j\|} = \frac{\mathbf{p}_i \mathbf{R}\mathbf{R}^T \mathbf{p}_j}{\|\mathbf{p}_i\| \|\mathbf{p}_j\|} = \cos(\theta_{ij}). \quad (10)$$

Singular Value Decomposition. We define two point clouds as \mathbf{P} and \mathbf{P}' ($\mathbf{P}, \mathbf{P}' \in \mathbb{R}^{N \times 3}$) with $\mathbf{P}' = \mathbf{P}\mathbf{R}$. Singular value decomposition is respectively performed as

$$\mathbf{U}\mathbf{\Sigma}\mathbf{V}^T = \mathbf{P}, \quad (11)$$

$$\mathbf{U}'\mathbf{\Sigma}'\mathbf{V}'^T = \mathbf{P}', \quad (12)$$

where \mathbf{U} and \mathbf{U}' are the eigenvector matrices of $\mathbf{P}\mathbf{P}^T$ and $\mathbf{P}'\mathbf{P}'^T$, respectively. $\mathbf{U} = \mathbf{U}'$ follows from the symmetry of $\mathbf{P}\mathbf{P}^T = \mathbf{P}'\mathbf{P}'^T$. The relationship between \mathbf{V} and \mathbf{V}' is able to be derived as $\mathbf{V}' = \mathbf{R}^T\mathbf{V}$. The invariance of point locations transformed by \mathbf{V} is then given by

$$\mathbf{P}'\mathbf{V}' = \mathbf{P}\mathbf{R}\mathbf{R}^T\mathbf{V} = \mathbf{P}\mathbf{V}, \quad (13)$$

4. Experimental Results

In this section, we report our experimental results on three popular datasets -i.e., ModelNet40 [44] (synthetic shape classification), ScanObjectNN [40] (real world shape classification), and ShapeNet [47] (part segmentation). Ablation studies are also included to better illustrate the contribution from each component in our network design.

4.1. Implementation Details

For local graph generation, we have used *k*-Nearest-Neighbor (kNN) search to find 32 neighbors for each central point. In global branch, we down sample the original model to a minimum of 32 points via farthest point sampling [28], and

an asymmetric edge function is also employed after the transformation as suggested in [42]. For further feature extraction, a series of MLPs with increasing dimensions (64, 128, 512, 1024) are employed. Each MLP is followed by Batch Normalization [17] and LeakyReLU [12]. We use three fully connected layers (512, 256, N_{cls}) to predict classification results, and three layers of MLPs (512, 256, N_{seg}) to generate segmentation results, where N_{cls} and N_{seg} denote the number of candidate labels in classification and segmentation, respectively. The network has been trained for 300 epochs on a NVIDIA TITAN XP GPU using Pytorch with SGD optimizer, learning rate 0.001, batch size 32, following the configuration in [42].

4.2. Experimental Setup

For a fair comparison, we divide previous methods into two categories, -i.e., rotation-sensitive and rotation-robust. The experiments are organized into three different conditions, -i.e., raw training data and testing data (z/z), raw training data and 3D rotation-augmented testing data ($z/SO3$), and 3D rotation-augmented training data and testing data ($SO3/SO3$). Note that $SO3$ means rotating raw point clouds along three axes, with the aim of taking rotation challenges into account, instead of data augmentation.

4.3. Synthetic Shape Classification

We evaluate our method on ModelNet40 which has been extensively used for synthetic shape classification [21, 18]. ModelNet40 includes 12311 CAD models from 40 categories that are split into 9843 for training and 2468 for testing. We randomly sample 1024 points from each model. These points are then centralized and normalized into a unit sphere.

Table 1 includes the experimental results for various experimental settings (two categories and three conditions). First, in the case of z/z , our method (LGR-Net) convincingly surpasses all other rotation-robust methods. When compared with Spherical-CNN [11] and a^3 S-CNN [24] where mesh reconstruction is required, our method achieves superior performance even though we only use raw points as input, which verifies our framework is more effective than spherical solutions. Compared with ClusterNet [5], Riconv [48], which also try to resolve the RI problem, our method still achieves better performance. It confirms that the presented local-global representation (LGR) is more effective. Second, in the situations of $z/SO3$ and $SO3/SO3$, the classification results of LGR-Net are close, outperforming other competitors by a large margin. By contrast, the results of rotation-sensitive algorithms considerably degrade. KPConv [39] that achieves outstanding performance with well-aligned data is vulnerable in $z/SO3$ and $SO3/SO3$. Specifically, it achieves a low accuracy (18.0%) in $z/SO3$ and its performance is still unsatisfying (87.4%) in $SO3/SO3$, even though the training data are augmented by 3D rotations. Moreover, We suggest [29, 31, 22, 42, 39] are still vulnerable against rotations when points and normals are immediately concatenated as input, because the normal direction is sensitive to rotation. PointNet ($xyz + normal$) is evaluated as an example: the accuracy is 15.9% in $z/SO3$, which does not look great when compared with PointNet (xyz) (16.4%).

In order to gain a deeper insight into the proposed method, we have calculated the confusion matrix as shown in Fig. 9. An interesting discovery is that ModelNet40 contains intrinsic ambiguity that has been overlooked in previous studies to the best of our knowledge. More specifically, as illustrated in Fig. 9, the most two confusing categories are flower pot and plant. The exemplar models belonging to these categories are provided, where both two models include similar plants and pots. Even for human observers, these two categories are difficult to distinguish; so it is reasonable for machine-based classification approaches to be confused by such intrinsic ambiguity.

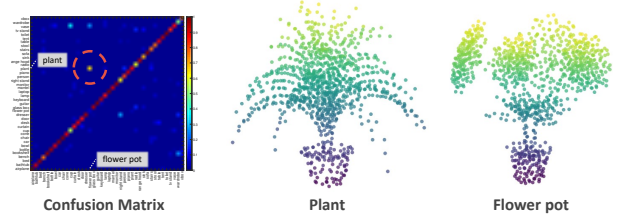


Figure 9: The overlooked intrinsic ambiguity in ModelNet40. The confusion matrix is calculated from the classification result of 40 candidate categories. The flower pot and plant are the most confusing categories (as verified by the confusion matrix). Both of them include similar plants and pots, which cannot be reliably classified even by human beings.

4.4. Real World Shape Classification

Considering that the objects in ModelNet40 are man-made CAD models (well-aligned and noise-free), there is a significant gap between synthetic data and real-world data. Real-world point clouds tend to include a variety of nuisances -e.g., missing data, occlusions, and non-uniform density. In order to evaluate rotation invariance in such conditions, we have conducted experiments on ScanObjectNN [40] which consists of real-world indoor scenes. This dataset includes 2902 objects which are classified into 15 categories. Some examples taken from this dataset are shown in Fig. 10.



Figure 10: Object examples in ScanObjectNN, where some typical nuisances, i.e., missing data, occlusions, and non-uniform density are included.

We have conducted the experiments on both the easiest subset OBJ_BG (without rotation, translation, and scaling) and the hardest subset PB_T50_RS (contains 50% bounding box translation, rotation around the gravity axis, and random scaling). Note that Spherical-CNN and a^3 S-CNN are not evaluated on this dataset because the required mesh data are unavailable; ClusterNet is unable to be retrained because of the unreleased code. The comparative results in terms of classification accuracy are shown in Table 2. In the cases of $z/SO3$ and $SO3/SO3$, our method achieves the best performance, which indicates that LGR-Net is not only invariant to rotation, but also

Methods	input	z/z(%)	z/SO3(%)	SO3/SO3(%)
Rotation-sensitive methods				
VoxNet [26]	volume	83.0	-	73.0
Subvolume [30]	volume	89.5	45.5	85.0
MVCNN [36]	image	90.2	81.5	86.0
PointNet [29] (<i>xyz</i>)	point	89.2	16.4	75.5
PointNet [29] (<i>xyz + normal</i>)	point	89.0	15.9	86.6
PointNet++ [31]	point	91.8	18.4	77.4
PointCNN [22]	point	91.3	41.2	84.5
DGCNN [42]	point	92.2	20.6	81.1
PointConv [43] (<i>xyz + normal</i>)	point	92.5	11.7	85.9
KPCConv [39]	point	92.7	18.0	87.4
Rotation-robust methods				
Spherical-CNN [11]	mesh	88.9	76.7	86.9
a^3 S-CNN [24]	mesh	89.6	87.9	88.7
ClusterNet [5]	point	87.1	87.1	87.1
Riconv [48]	point	86.5	86.4	86.4
LGR-Net	point	90.9	90.9	91.1

Table 1: Synthetic shape classification results on ModelNet40. The evaluated approaches are divided into the rotation-sensitive method and rotation-robust method. The experiments are performed in three situations based on different combinations of training data and testing data. z and $S03$ are respectively represent raw data and 3D rotation-augmented data. The metric is classification accuracy and the best result is rendered in bold.

robust to typical nuisances, i.e., missing data, occlusions, and non-uniform density.

4.5. Part Segmentation

Given a point cloud model, the objective of segmentation is to accurately predict per-point labels. When compared with the shape classification, segmentation is more challenging because it involves the discrimination of fine-detailed structures. We have extended our experiments on ShapeNet [47] - a widely used dataset for evaluating part segmentation. We have considered a subset of ShapeNet including 16881 3D models, 16 kinds of objects, and 50 part categories. The average category mIoU (Cat. mIoU) [33] is utilized to compare the segmentation performance.

Specific results in two different cases are shown in Table 3. In the case of $z/S03$, our LGR-Net dramatically surpasses the previous rotation-robust method Riconv (ours behaves better in 15 categories out of 16 ones in total). In $S03/S03$, LGR-Net achieves the most consistent performance, significantly exceeding other methods (for 12 out of 16 categories, ours achieves the best or the second best result). The overall comparison results are reported in Table 4, which clearly justify the superiority of LGR-Net.

Some representative visualization results for part segmentation on ShapeNet are shown in Fig. 11. The training data are rotation-free, while the testing data are transformed by the specific 3D rotation, -i.e., ($45^\circ, 45^\circ, 45^\circ$). It can be easily observed that our approach (LGR-Net) significantly outperforms the competing methods (PointNet [29] and Riconv [48]). Our part segmentation results are visually closer to the ground-truth in all 16 different cases.

4.6. 3D Scene Segmentation

To shed more light on the effectiveness of our method in real-world applications, we perform experiments on S3DIS [3],

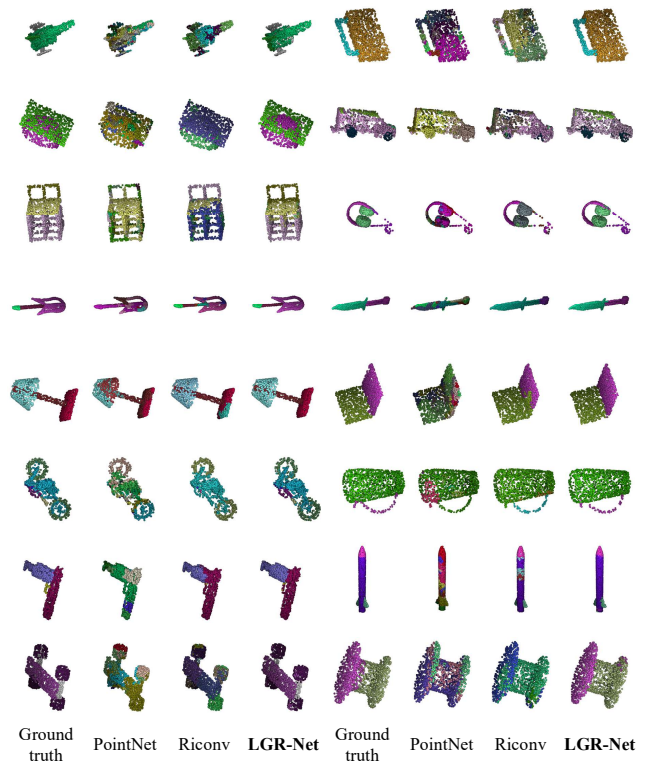


Figure 11: Visualization results for part segmentation. The networks are trained and tested on ShapeNet, and different parts are represented by different colors. The training data are rotation-free, while the testing data are transformed by the specific 3D rotation, -i.e., ($45^\circ, 45^\circ, 45^\circ$).

which has been widely used as a benchmark of 3D Scene segmentation. Specifically, S3DIS includes 273 million points in total, which are sampled from six large-scale indoor areas and divided into 13 classes. We employ Area-5 for testing

Methods	OBJ_BG (%)			PB_T50_RS (%)		
	z/z	z/SO3	SO3/SO3	z/z	z/SO3	SO3/SO3
Rotation-sensitive methods						
PointNet [29]	73.3	16.7	54.7	68.2	17.1	42.2
PointNet++ [31]	82.3	15.0	47.4	77.9	15.8	60.1
PointCNN [22]	86.1	14.6	63.7	78.5	14.9	51.8
DGCNN [42]	82.8	17.7	71.8	78.1	16.1	63.4
Rotation-robust methods						
Riconv [48]	78.4	78.4	78.1	67.9	67.9	68.3
LGR-Net	81.2	81.2	81.4	72.7	72.7	72.9

Table 2: Real world shape classification results on ScanObjectNN. Two parts, -i.e., OBJ_BG and PB_T50_RS are considered. OBJ_BG contains objects and backgrounds without rotation, translation, and scaling; while PB_T50_RS takes into account of 50% bounding box translation, rotation around the gravity axis, and random scaling. The performance is measured by classification accuracy.

#shapes	aero	bag	cap	car	chair	earph.	guitar	knife	lamp	laptop	motor	mug	pistol	rocket	skate	table
	2690	76	55	898	3758	69	787	392	1547	451	202	184	283	66	152	5271
<i>z/SO3(%)</i>																
PointNet [29]	40.4	48.1	46.3	24.5	45.1	39.4	29.2	42.6	52.7	36.7	21.2	55.0	29.7	26.6	32.1	35.8
PointNet++ [31]	51.3	66.0	50.8	25.2	66.7	27.7	29.7	65.6	59.7	70.1	17.2	67.3	49.9	23.4	43.8	57.6
PointCNN [22]	21.8	52.0	52.1	23.6	29.4	18.2	40.7	36.9	51.1	33.1	18.9	48.0	23.0	27.7	38.6	39.9
DGCNN [42]	37.0	50.2	38.5	24.1	43.9	32.3	23.7	48.6	54.8	28.7	17.8	74.4	25.2	24.1	43.1	32.3
Riconv [48]	<u>80.6</u>	<u>80.0</u>	<u>70.8</u>	<u>68.8</u>	<u>86.8</u>	<u>70.3</u>	<u>87.3</u>	84.7	<u>77.8</u>	80.6	<u>57.4</u>	<u>91.2</u>	<u>71.5</u>	<u>52.3</u>	<u>66.5</u>	<u>78.4</u>
LGR-Net	81.5	80.5	81.4	75.5	87.4	72.6	88.7	83.4	83.1	86.8	66.2	92.9	76.8	62.9	80.0	80.0
<i>SO3/SO3(%)</i>																
PointNet [29]	<u>81.6</u>	68.7	74.0	70.3	<u>87.6</u>	68.5	<u>88.9</u>	80.0	74.9	83.6	56.5	77.6	75.2	<u>53.9</u>	69.4	79.9
PointNet++ [31]	79.5	71.6	87.7	<u>70.7</u>	88.8	64.9	88.8	78.1	79.2	94.9	54.3	<u>92.0</u>	76.4	50.3	68.4	81.0
PointCNN [22]	78.0	<u>80.1</u>	78.2	<u>68.2</u>	81.2	70.2	82.0	70.6	68.9	80.8	48.6	<u>77.3</u>	63.2	50.6	63.2	82.0
DGCNN [42]	77.7	71.8	77.7	55.2	87.3	68.7	88.7	<u>85.5</u>	81.8	81.3	36.2	86.0	<u>77.3</u>	51.6	65.3	80.2
Riconv [48]	80.6	80.2	70.7	68.8	86.8	70.4	87.2	<u>84.3</u>	78.0	80.1	<u>57.3</u>	91.2	71.3	52.1	66.6	78.5
LGR-Net	81.7	78.1	<u>82.5</u>	75.1	<u>87.6</u>	74.5	89.4	86.1	83.0	86.4	65.3	92.6	75.2	64.1	79.8	80.5

Table 3: Specific per-class average mIoU in the cases of *z/SO3* and *SO3/SO3* (**bold** - the best, underline - the second best).

Methods	z/z (%)	z/SO3 (%)	SO3/SO3 (%)
Rotation-sensitive methods			
PointNet [29]	80.4	37.8	74.4
PointNet++ [31]	81.9	48.2	76.7
PointCNN [22]	84.6	34.7	71.4
DGCNN [42]	82.3	37.4	73.3
Rotation-robust methods			
Riconv [48]	74.6	75.3	75.5
LGR-Net	80.0	80.0	80.1

Table 4: Overall part segmentation results on ShapeNet. The metric is overall average category mIoU (Cat. mIoU) estimated by averaging the results over 16 categories.

and use the other five areas for training, following the settings in [38, 39]. Since normals are not provided on S3DIS, we take the distances coupled with RGB features as input in our local branch.

As reported in Table 5, the rotation-sensitive methods are vulnerable against rotations on S3DIS. The mIoU of DGCNN drops by 44.8% when rotations are taken into account, i.e., from 48.4% in *z/z* to 3.6% in *z/SO3*. The performance is still limited in *SO3/SO3*, i.e., 34.3%, even though the training data are 3D rotation-augmented. By contrast, our LGR-Net achieves superior results when facing the challenge of rotations, outper-

forming the previous rotation-robust method, i.e., Riconv, by 21.4%. Moreover, since our global rotation-invariant features are extracted based on SVD on down-sampled 32 points (default setting), one may concern if the presented global RI features are effective on large-scale point clouds. To address this issue, we perform an ablation study on S3DIS, which removes global branch from the proposed network and only takes the local RI features as input. Empirically, we found the removing of global branch results in 7.0% mIoU decrease, i.e., from 43.4% to 36.4%. It demonstrates that the global branch still plays an important role in 3D scene segmentation.

Methods	z/z (%)	z/SO3 (%)	SO3/SO3 (%)
Rotation-sensitive methods			
PointNet [29]	41.1	4.1	29.3
DGCNN [42]	48.4	3.6	34.3
Rotation-robust methods			
Riconv [48]	22.0	22.0	22.0
LGR-Net	43.4	43.4	43.4

Table 5: 3D scene segmentation results (mIoU) on S3DIS Area-5 [3].

4.7. Robustness against sampling rates and strategies

Since our global RI representation is generated on three orthogonal axes which are estimated by SVD on a down-

sampling structure, the robustness of SVD against different down-sampling rates and strategies is critical for our method. To address this issue, we evaluate LGR-Net on *OBJ_BG* of ScanObjectNN, employing two different down-sampling strategies and three down-sampling rates. The results are shown in Table 6. Under different down-sampling strategies and down-

Sampling strategy	# points		
	8	16	32
Random sampling (%)	79.0	79.0	80.9
Farthest point sampling (%)	78.0	80.7	81.2

Table 6: Analysis of robustness of SVD against sampling rates and strategies on *OBJ_BG*. We sample 32 points at most because of the computational cost.

sampling rates, our method still outperforms RiConv (78.4%) in most cases, which justifies that our global RI representation is robust to sampling strategies and sampling rates.

4.8. Ablation Studies

Ablation studies are performed to demonstrate the rationality of our network design. Specifically, we separately train the global branch and local branch of the LGR-Net classification network on *OBJ_BG* of ScanObjectNN. We also train two other versions, replacing attention-based fusion module by an ad-hoc average pooling layer (Avg-Pool) and concatenation-and-convolution processing (Cat-Conv), respectively. As shown in Table 7 and Table 8, the results suggest that both branches and attention-based fusion have positive impacts on LGR-Net. The two branches contain complementary information -i.e., local geometry and global topology; attention-based fusion is capable of combining them adaptively and making the feature fusion process more reasonable.

Global Branch	Local Branch	Attention Fusion	Accuracy (%)
✓	×	×	71.6
×	✓	×	71.3
✓	✓	×	80.6
✓	✓	✓	81.2

Table 7: Ablation studies of LGR-Net on *OBJ_BG*.

Method	Avg-Pool	Cat-Conv	Attention
Accuracy (%)	80.6	80.2	81.2

Table 8: Analysis of fusion methods, where Cat-Conv concatenates two-branch features and then fuses the features by a convolution layer.

We have implemented an one-branch version at the early stage of this work, which projects all points into the estimated global coordinate system and then performs local feature extraction (One-Branch Network). This one-branch version has been abandoned because we are motivated by the observation that local and global information are supposed to play complementary roles in different regions. Consequently, it is more reasonable to separately extract local and global information in

Method	z/z (%)	z/SO3 (%)	SO3/SO3 (%)
One-Branch Network	78.7	78.7	79.2
LGR-Net	81.2	81.2	81.4

Table 9: Analysis of the two-branch design on *OBJ_BG*. The one-branch version projects all points into the estimated global coordinate system and then performs local feature extraction.

a two-branch architecture and fuse the feature maps in an adaptive manner. The results of One-Branch Network and LGR-Net on *OBJ_BG* of ScanObjectNN are shown in Table 9. Compared with One-Branch Network, LGR-Net performs better in all three cases. The experimental results have justified the superiority of our new two-branch design.

5. Limitations and Discussions

To analyze limitations of our method, we replace RI representations in the global branch with well-aligned point coordinates. The performance on the rotation-free version of *OBJ_BG* significantly increases (around 6%). Based on such observation, we discuss two limitations of our global RI representations as follows.

First, considering that the objects in existing datasets are well-aligned, the poses among different instances from the same category are consistent, which provide an underlying consistency for learning. Although the projected poses in the global branch are invariant to rotation, we find that the orientations of objects in the same category are not quite consistent, increasing the difficulty of learning. A method which is not only invariant to rotation but also can align instances from the same category to a consistent orientation is desired in our further work.

Second, real-world point cloud data are at the mercy of noise contamination and missing data (e.g., due to the occlusion or reflection from specular surfaces). Orientations determined by SVD can be affected by such nuisances. At present, we alleviate this issue by performing SVD on down-sampled skeleton-like structures which exhibit certain robustness against noise and missing data. Nonetheless, how to overcome the influence of such nuisances remains an important direction for improving our work.

Although LGR-Net has above-mentioned limitations, we have achieved a better trade-off between the accuracy/mIoU and rotation invariance when compared with other competing methods as confirmed by experimental results in Sec. 4.

6. Conclusion

We have presented RI representations in terms of local geometry and global topology for point cloud analysis. With RI feature extraction, we integrate the representations into a two-branch network, where an attention-based fusion module is designed to adaptively fuse two-branch features. Both theoretical and empirical proofs for RI are provided. Experimental results have demonstrated the superiority of our network design to other competing approaches. In our future works, we expect

to study the adaptation of LGR-Net to large-scale datasets (e.g., KITTI) to facilitate other point cloud based vision tasks such as LiDAR SLAM and autonomous driving.

Acknowledgment

This work was supported in part by the National Natural Science Foundation of China under Grant 61876211 and by the 111 Project on Computational Intelligence and Intelligent Control under Grant B18024. Xin Li's work is partially supported by the DoJ/NIJ under grant NIJ 2018-75-CX-0032, NSF under grant OAC-1839909, IIS-1951504 and the WV Higher Education Policy Commission Grant (HEPC.dsr.18.5).

References

- [1] Alexiou, E., Upenik, E., Ebrahimi, T., 2017. Towards subjective quality assessment of point cloud imaging in augmented reality, in: Proceedings of the IEEE International Workshop on Multimedia Signal Processing, IEEE. pp. 1–6.
- [2] Altmann, S.L., 2005. Rotations, quaternions, and double groups. Courier Corporation.
- [3] Armeni, I., Sener, O., Zamir, A.R., Jiang, H., Brilakis, I., Fischer, M., Savarese, S., 2016. 3d semantic parsing of large-scale indoor spaces, in: Proceedings of the IEEE Conference on Computer Vision and Pattern Recognition, pp. 1534–1543.
- [4] Bailey, T., Durrant-Whyte, H., 2006. Simultaneous localization and mapping (slam): Part ii. IEEE Robotics & Automation Magazine 13, 108–117.
- [5] Chen, C., Li, G., Xu, R., Chen, T., Wang, M., Lin, L., 2019. Cluster-net: Deep hierarchical cluster network with rigorously rotation-invariant representation for point cloud analysis, in: Proceedings of the IEEE Conference on Computer Vision and Pattern Recognition, pp. 4994–5002.
- [6] Cheng, H., Chung, S.M., 2016. Orthogonal moment-based descriptors for pose shape query on 3d point cloud patches. Pattern Recognition 52, 397–409.
- [7] Cohen, T.S., Geiger, M., Köhler, J., Welling, M., 2018. Spherical cnns, in: International Conference on Learning Representations.
- [8] Deng, H., Birdal, T., Ilic, S., 2018. Ppf-foldnet: Unsupervised learning of rotation invariant 3d local descriptors, in: Proceedings of the European Conference on Computer Vision, pp. 602–618.
- [9] Deng, J., Dong, W., Socher, R., Li, L.J., Li, K., Fei-Fei, L., 2009. Imagenet: A large-scale hierarchical image database, in: Proceedings of the IEEE Conference on Computer Vision and Pattern Recognition, Ieee. pp. 248–255.
- [10] Durrant-Whyte, H., Bailey, T., 2006. Simultaneous localization and mapping: part i. IEEE Robotics & Automation Magazine 13, 99–110.
- [11] Esteves, C., Allen-Blanchette, C., Makadia, A., Daniilidis, K., 2018. Learning so (3) equivariant representations with spherical cnns, in: Proceedings of the European Conference on Computer Vision, pp. 52–68.
- [12] Glorot, X., Bordes, A., Bengio, Y., 2011. Deep sparse rectifier neural networks, in: Proceedings of the International Conference on Artificial Intelligence and Statistics, pp. 315–323.
- [13] Golub, G.H., Reinsch, C., 1971. Singular value decomposition and least squares solutions, in: Linear Algebra. Springer, pp. 134–151.
- [14] He, K., Zhang, X., Ren, S., Sun, J., 2016. Deep residual learning for image recognition, in: Proceedings of the IEEE Conference on Computer Vision and Pattern Recognition, pp. 770–778.
- [15] Hori, C., Hori, T., Lee, T.Y., Zhang, Z., Harsham, B., Hershey, J.R., Marks, T.K., Sumi, K., 2017. Attention-based multimodal fusion for video description, in: Proceedings of the IEEE international conference on computer vision, pp. 4193–4202.
- [16] Huang, H., Wu, S., Cohen-Or, D., Gong, M., Zhang, H., Li, G., Chen, B., 2013. L1-medial skeleton of point cloud. ACM Trans. Graph. 32, 65–1.
- [17] Ioffe, S., Szegedy, C., 2015. Batch normalization: Accelerating deep network training by reducing internal covariate shift. ArXiv preprint arXiv:1502.03167 .
- [18] Jiang, M., Wu, Y., Zhao, T., Zhao, Z., Lu, C., 2018. Pointsift: A sift-like network module for 3d point cloud semantic segmentation. ArXiv preprint arXiv:1807.00652 .
- [19] Kazhdan, M., Funkhouser, T., Rusinkiewicz, S., 2003. Rotation invariant spherical harmonic representation of 3 d shape descriptors, in: Symposium on geometry processing, pp. 156–164.
- [20] Li, B., Ouyang, W., Sheng, L., Zeng, X., Wang, X., 2019. Gs3d: An efficient 3d object detection framework for autonomous driving, in: Proceedings of the IEEE Conference on Computer Vision and Pattern Recognition, pp. 1019–1028.
- [21] Li, J., Chen, B.M., Hee Lee, G., 2018a. So-net: Self-organizing network for point cloud analysis, in: Proceedings of the IEEE Conference on Computer Vision and Pattern Recognition, pp. 9397–9406.
- [22] Li, Y., Bu, R., Sun, M., Wu, W., Di, X., Chen, B., 2018b. Pointcnn: Convolution on x-transformed points, in: Advances in Neural Information Processing Systems, pp. 820–830.
- [23] Limberger, F.A., Oliveira, M.M., 2015. Real-time detection of planar regions in unorganized point clouds. Pattern Recognition 48, 2043–2053.
- [24] Liu, M., Yao, F., Choi, C., Sinha, A., Ramani, K., 2018. Deep learning 3d shapes using alt-az anisotropic 2-sphere convolution, in: International Conference on Learning Representations.
- [25] Maaten, L.v.d., Hinton, G., 2008. Visualizing data using t-sne. Journal of Machine Learning Research 9, 2579–2605.
- [26] Maturana, D., Scherer, S., 2015. Voxnet: A 3d convolutional neural network for real-time object recognition, in: IEEE/RSJ International Conference on Intelligent Robots and Systems, IEEE. pp. 922–928.
- [27] Meyer, G.P., Laddha, A., Kee, E., Vallespi-Gonzalez, C., Wellington, C.K., 2019. Lasernet: An efficient probabilistic 3d object detector for autonomous driving, in: Proceedings of the IEEE Conference on Computer Vision and Pattern Recognition, pp. 12677–12686.
- [28] Moenning, C., Dodgson, N.A., 2003. Fast marching farthest point sampling. Technical Report. University of Cambridge, Computer Laboratory.
- [29] Qi, C.R., Su, H., Mo, K., Guibas, L.J., 2017a. Pointnet: Deep learning on point sets for 3d classification and segmentation, in: Proceedings of the IEEE Conference on Computer Vision and Pattern Recognition, pp. 652–660.
- [30] Qi, C.R., Su, H., Nießner, M., Dai, A., Yan, M., Guibas, L.J., 2016. Volumetric and multi-view cnns for object classification on 3d data, in: Proceedings of the IEEE Conference on Computer Vision and Pattern Recognition, pp. 5648–5656.
- [31] Qi, C.R., Yi, L., Su, H., Guibas, L.J., 2017b. Pointnet++: Deep hierarchical feature learning on point sets in a metric space, in: Advances in Neural Information Processing Systems, pp. 5099–5108.
- [32] Rusu, R.B., Blodow, N., Marton, Z.C., Beetz, M., 2008. Aligning point cloud views using persistent feature histograms, in: IEEE/RSJ International Conference on Intelligent Robots and Systems, IEEE. pp. 3384–3391.
- [33] Shen, Y., Feng, C., Yang, Y., Tian, D., 2018. Mining point cloud local structures by kernel correlation and graph pooling, in: Proceedings of the IEEE Conference on Computer Vision and Pattern Recognition, pp. 4548–4557.
- [34] Simonyan, K., Zisserman, A., 2014. Very deep convolutional networks for large-scale image recognition. ArXiv preprint arXiv:1409.1556 .
- [35] Spivak, M.D., 1970. A comprehensive introduction to differential geometry. Publish or perish.
- [36] Su, H., Maji, S., Kalogerakis, E., Learned-Miller, E., 2015. Multi-view convolutional neural networks for 3d shape recognition, in: Proceedings of the IEEE International Conference on Computer Vision, pp. 945–953.
- [37] Tagliasacchi, A., Zhang, H., Cohen-Or, D., 2009. Curve skeleton extraction from incomplete point cloud, in: ACM SIGGRAPH 2009 papers, pp. 1–9.
- [38] Tchapmi, L., Choy, C., Armeni, I., Gwak, J., Savarese, S., 2017. Seg-cloud: Semantic segmentation of 3d point clouds, in: International conference on 3D vision, IEEE. pp. 537–547.
- [39] Thomas, H., Qi, C.R., Deschaud, J.E., Marcotegui, B., Goulette, F., Guibas, L.J., 2019. Kpconv: Flexible and deformable convolution for point clouds, in: Proceedings of the IEEE Conference on Computer Vision and Pattern Recognition, pp. 6411–6420.
- [40] Uy, M.A., Pham, Q.H., Hua, B.S., Nguyen, D.T., Yeung, S.K., 2019. Revisiting point cloud classification: A new benchmark dataset and classification model on real-world data. ArXiv preprint arXiv:1908.04616

- [41] Wang, Q., Ronneberger, O., Burkhardt, H., 2009. Rotational invariance based on fourier analysis in polar and spherical coordinates. *IEEE Transactions on Pattern Analysis and Machine Intelligence* 31, 1715–1722.
- [42] Wang, Y., Sun, Y., Liu, Z., Sarma, S.E., Bronstein, M.M., Solomon, J.M., 2019. Dynamic graph cnn for learning on point clouds. *ACM Transactions on Graphics* 38, 146.
- [43] Wu, W., Qi, Z., Fuxin, L., 2019. Pointconv: Deep convolutional networks on 3d point clouds, in: *Proceedings of the IEEE Conference on Computer Vision and Pattern Recognition*, pp. 9621–9630.
- [44] Wu, Z., Song, S., Khosla, A., Yu, F., Zhang, L., Tang, X., Xiao, J., 2015. 3d shapenets: A deep representation for volumetric shapes, in: *Proceedings of the IEEE Conference on Computer Vision and Pattern Recognition*, pp. 1912–1920.
- [45] Xu, Y., Fan, T., Xu, M., Zeng, L., Qiao, Y., 2018. Spidernn: Deep learning on point sets with parameterized convolutional filters, in: *Proceedings of the European Conference on Computer Vision*, pp. 87–102.
- [46] Yang, Z., Sun, Y., Liu, S., Shen, X., Jia, J., 2018. Ipod: Intensive point-based object detector for point cloud. *ArXiv preprint arXiv:1812.05276*
- [47] Yi, L., Kim, V.G., Ceylan, D., Shen, I., Yan, M., Su, H., Lu, C., Huang, Q., Sheffer, A., Guibas, L., et al., 2016. A scalable active framework for region annotation in 3d shape collections. *ACM Transactions on Graphics* 35, 210.
- [48] Zhang, Z., Hua, B.S., Rosen, D.W., Yeung, S.K., 2019. Rotation invariant convolutions for 3d point clouds deep learning. *ArXiv preprint arXiv:1908.06297*